STUDY OF BASIN SCALE ACOUSTIC TRANSMISSIONS

by

John Richard Nystrom

B.S. Computer Science
University of Idaho (1990)

Submitted in partial fulfillment of the
requirements for the degree of

MASTER OF SCIENCE IN OCEAN ENGINEERING

at the

MASSACHUSETTS INSTITUTE OF TECHNOLOGY

and the

WOODS HOLE OCEANOGRAPHIC INSTITUTION

September 1992

Signature of Author .....
Joint Program in Applied Ocean Science and Engineering
Massachusetts Institute of Technology
Woods Hole Oceanographic Institution
August 1, 1992

Certified by .....
Dr. John L. Spiesberger
Associate Scientist
Woods Hole Oceanographic Institution
Thesis Co-Supervisor

Certified by .....
Dr. Beth Chertock
Oceanographer
NOAA Environmental Research Laboratories
Wave Propagation Laboratory
Thesis Co-Supervisor

Accepted by .....
Dr. Arthur B. Baggeroer
Chairman, Joint Committee for Applied Ocean Science and Engineering
Massachusetts Institute of Technology/
Woods Hole Oceanographic Institute

STUDY OF BASIN SCALE ACOUSTIC TRANSMISSIONS

by

John Richard Nystrom

Submitted to the Massachusetts Institute of Technology/
Woods Hole Oceanographic Institution
Joint Program in Applied Ocean Science and Engineering
on August 1, 1992, in partial fulfillment of the
requirements for the degree of
Master of Science in Ocean Engineering

ABSTRACT

A basin-scale acoustic tomography experiment was conducted in the northeast Pacific from May 1987 to September 1987. In this thesis, the stability of the forward model is analyzed. There are large non-linearities in the changes in travel time between ray paths for the four seasons. I constructed a model in which the change in warming in the upper 100 m of the ocean was due only to changes in surface solar irradiance. The value of the surface solar irradiance anomalies necessary to cause the tomography results for warming (Spiesberger and Metzger, 1991) was computed. This value was larger than the actual value of surface solar irradiance anomaly which was computed using inputs measured by satellite (Chertock, 1989).

Thesis Supervisors: Dr. John L. Spiesberger
Woods Hole Oceanographic Institution

Dr. Beth Chertock
NOAA Environmental Research Laboratories
Wave Propagation Laboratory

ACKNOWLEDGEMENTS

I owe many thanks to my advisors, Dr. John Spiesberger and Dr. Beth Chertock; without their guidance, support and encouragement this thesis could not have been written.

I am appreciative of Marga McElroy and Lee Freitag for their effort, help and friendship.

I am indebted to the US Navy for allowing me to continue my education.

I would like to thank Gary Edwards for his friendship and advice.

I want to thank Cleo for her friendship.

I am grateful to my fellow graduate students for their support and friendship.

Finally, and most importantly, I want to express my deepest gratitude for my family's love, devotion, patience, support and understanding. I could not have made it without them.

CONTENTS

LIST OF FIGURES

LIST OF TABLES

Chapter I

Introduction

1.1 Motivation and Overview

Measurement of basin scale changes in ocean temperature, at the surface and in the interior, is an important step in detecting global climate changes. Long range ocean acoustic tomography is an important tool for measuring the internal variability (Spiesberger and Metzger, 1991; Spiesberger et al., 1992). Satellites are an important tool in measuring basin-wide variations of temperature and radiation at the sea surface (Stewart, 1985). This thesis compares changes in basin-wide temperature in the interior with changes at the surface. I compute the surface solar irradiance anomalies necessary to achieve the topographically derived warming rate anomalies in the upper 100 m of the ocean along the experiment's path. The computation is based on a model in which the change in warming is due only to changes in surface solar irradiance anomalies. This thesis also investigates the stability of the models used to trace sound through the ocean.

This thesis provides an introduction to tomography and to surface solar irradiance at the oceans surface in chapter I. Chapter II describes the forward model, examines the stability of the model from season to season, and compares the model to the experimental data. Chapter III examines the estimate of

the surface solar irradiance anomalies and how it is computed Results and conclusions are given in chapter IV.

1.2 Acoustic Tomography

It is difficult to obtain time and space data coverage of the ocean by most traditional observational methods. Shipboard sensors can only measure one point of an observational area at a given time, and must move around the area taking many measurements to get good spatial data coverage. This can provide poor temporal resolution because the parameters being measured change during the ship's movements. Point measurements made by moored sensors provide good temporal resolution of one point over time, but providing sufficient areal coverage requires many such moorings.

Ocean acoustic tomography was first proposed by Walter Munk and Carl Wunsch(1979) for measuring mesoscale(~100 km) processes. It is a method of determining oceanic structure and variability through the inversion of acoustic travel-times to determine perturbations in sound-speed and currents and thus perturbations in temperature and density. Ocean acoustic tomography experiments are conducted by placing acoustic sources and receivers in the ocean. Each source transmits a pulse which is received at each receiver. The travel-time for each ray path is compared to the computed value for a model of known sound-speeds and the system is then "inverted" to

estimate the sound-speed anomalies.

One of the big advantages of tomography is that relatively few instruments are required to get good areal coverage of a large ocean area. If **S** sources and **R** receivers are placed around a volume and if **P** multipaths can be identified between them then there are **S x R x P** pieces of data per measurement. If point measurements are used then there is only one datum per instrument(**S + R** data) at one time. Because sound travels at about 1500 m s^{-1} in the ocean the time to collect the tomography data is relatively short and thus can give a three dimensional synoptic measurement of oceanic parameters.

Ocean acoustic tomography was successfully used in a 1981 acoustic tomography experiment(Cornuelle et al., 1982; 1985) to map sound-speed anomalies on a 300 km square area near Bermuda. A 1981 experiment (Spiesberger et al., 1983) measured Gulf Stream meanders. The 1987 experiment by Spiesberger and Metzger (1991) and the 1983-1984 experiment by Spiesberger et al. (1992) demonstrated the use of sound to observe temperature fluctuations over ocean basins (to 4000km).

1.3 Surface Solar Irradiance

The short wave radiation from the sun that is absorbed by the ocean, surface solar irradiance (Q_L), is an important part of the heat balance of the atmosphere and the ocean. The other terms in the balance are latent and sensible heat fluxes and

outgoing long-wave radiation. The long-wave radiation from the ocean, Q_B, can be estimated using the formula (Gill, 1992),

$$Q_B = 0.985\sigma T_s^4 (0.39 - 0.05 e_a^{1/2}) (1 - 0.6 n_c^2) \qquad \textbf{(1.1)}$$

where σ is Stephen's constant for a black body, T_S(°K) is temperature, e_a is the vapor pressure of water at the standard height(mb), n_c is the fraction of sky covered by clouds, and the last factor,$(1 - 0.6n_c^2)$, is a correction for clouds. The total upward flux of heat, Q, from the ocean is the sum of the fluxes of the individual processes, namely (Gill, 1982):

$$Q = Q_B + L_V E + Q_s - Q_L \qquad \textbf{(1.2)}$$

where Q_L is the surface solar irradiance, for our purposes, computed by Chertock's algorithm(1989). Q_s is the upward sensible heat flux, and $L_V E$ the upward latent heat flux, with E the evaporation rate, and L_V the latent heat of vaporization of water given by

$$L_v = 2.5 \times 10^6 \; J \; kg^{-1} \; . \qquad \textbf{(1.3)}$$

A simple model is used in this thesis to describe warming anomalies in the upper 100 m along the experiment's path. The model considers surface solar irradiance anomalies as the only source of warming anomalies. The other terms in the heat budget are not considered, including advection. I will use this model to quantify the magnitude of the surface solar irradiance anomaly necessary to cause the warming observed by tomography.

Chapter II

Travel-Time Changes

2.1 The Experiment

The experiment used three acoustic sources and seven receivers. The sources were deployed in a triangle, approximately 1000 km on a side, north of Hawaii (Figure 2.1). Source (S1) was deployed in about 5500 m of water on a taunt mooring at 667 m depth. It transmitted every 2 hours, 12 times a day, every fourth day. The pulse-like signal's acoustic frequency was centered at 250 Hz with an rms bandwidth of 63 Hz. Thus it had a pulse resolution of $(63\text{Hz})^{-1} \approx 16$ ms (Spiesberger and Metzger, 1991). The source level was 191 dB re 1 μPa @1m. The time of the source transmission of the signal is known to about 1 ms with the use of a rubidium frequency standard. The time was known to the same accuracy at the receiver. The geographic positions of the sources were measured to an accuracy of about 10 m with the Global Positioning System. Mooring motion was tracked with the use of four bottom-mounted transponders and an interrogator on the mooring near the source (Liberatore, 1985). The receivers are bottom mounted off the west coast of the United States. Their positions are known to an accuracy of about 120 m (Spiesberger and Metzger, 1991).

The Acoustic path I studied extends over about 2000 km and

was insonified for 120 days from May 1987 to September 1987. It was necessary to raise the SNR (Signal to Noise Ratio) because the source could not transmit a pulse powerful enough to be heard above the background noise level. The SNR was increased about 36 dB when the received acoustic signal was complex demodulated, low-passed filtered, correlated with a replica (phase-only-filtering), and averaged over four sequence periods (Spiesberger et al., 1989). The data were corrected for mooring motion and clock drift to within the limits noted above. The source used for this experiment is designated S1 and the receiver is designated R1 on Figure 2.1. Source S3 and receiver R2 were used by Spiesberger and Metzger (1991).

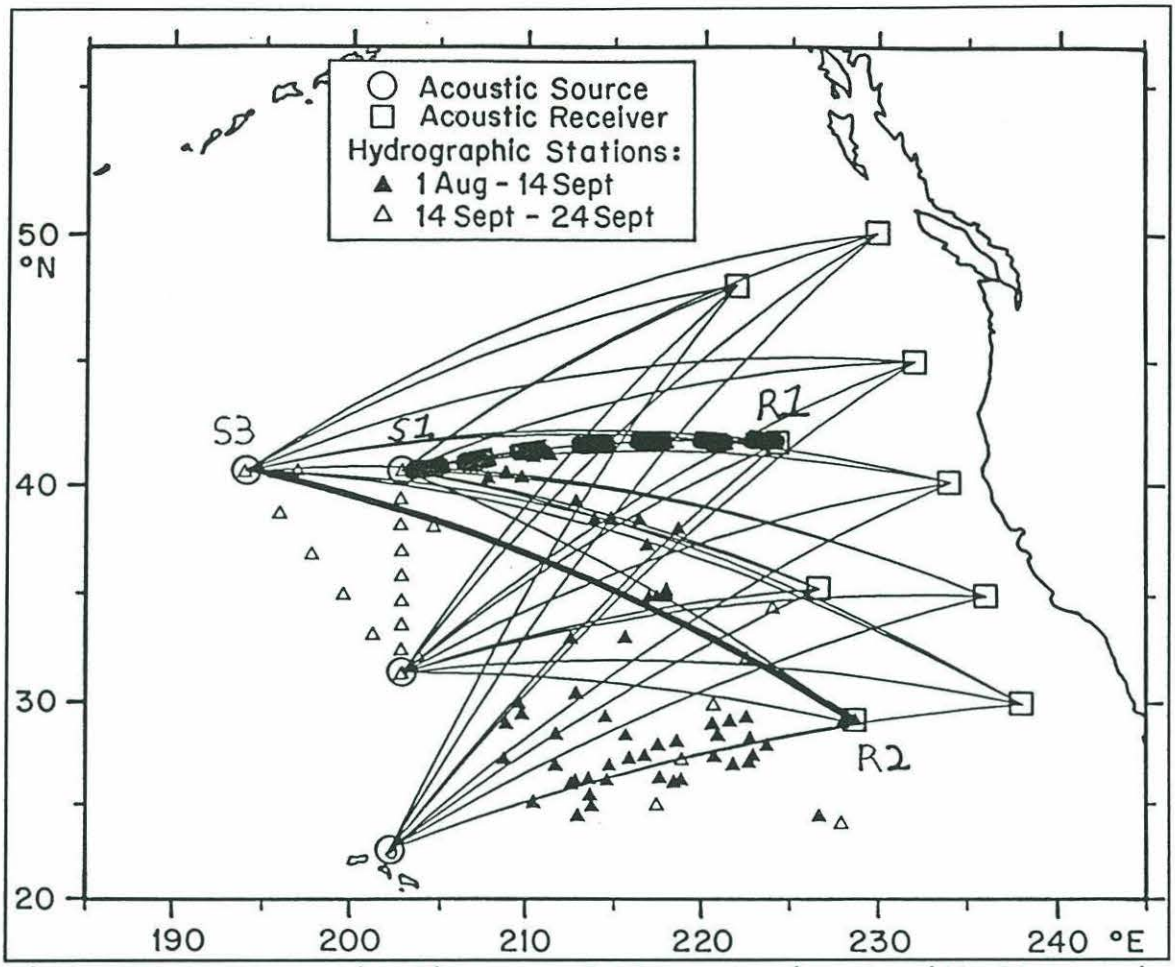

Figure 2.1 Schematic diagram of the experiment with the position of the sources and receivers indicated. The acoustic path used in this paper is indicated with the heavy dashed line. From Spiesberger and Metzger, 1991.

2.2 Ray Tracing

The speed of sound in the ocean depends on temperature, pressure, and salinity. Del Grosso's (1974) algorithm for sound-speed in sea water is,

$$c_{STP} = c_{000} + \Delta c_t + \Delta c_s + \Delta c_P + \Delta c_{STP} \qquad \textbf{(2.1)}$$

where,

$$c_{000} = 1402.392$$
$$\Delta c_T = 5.01109T - .550946x10^{-1}T^2 + .2215153X10^{-3}T^3$$
$$\Delta c_S = 1.32952S + .128955X10^{-3}S^2$$
$$\Delta c_P = .156059P + .244998X10^{-4}P^2 - .883392X10^{-8}P^3$$
$$\Delta c_{STP} = -.127x10^{-1}TS + .635X10^{-2}TP + .2654X10^{-7}T^2P^2$$
$$-.159x10^{-5}TP^2 + .522X10^{-9}TP^3 - .438X10-6T^3P$$
$$-.161X10^{-8}S^2P^2 + .968X10^{-4}T^2S + .485X10^{-5}TS^2P$$
$$-.340X10^{-3}TSP$$

where T is temperature in degrees Celsius, S is salinity in parts per thousand, and P is pressure in kilograms per square centimeter. Temperature and pressure have a much greater effect than salinity on sound-speed in most regions of the ocean.

We will now develop a solution to the acoustic wave equation in terms of ray theory. The wave equation is (Tolstoy and Clay, 1966)

$$\nabla^2 p - \frac{1}{c^2}\frac{\partial^2 p}{\partial t^2} = 0 \qquad \textbf{(2.2)}$$

where ∇^2 is the Laplacian operator, p is the acoustic pressure and c is the sound-speed, a function of salinity, pressure, and temperature which may vary with spatial coordinates(i.e., **c** = c(x,y,z)). For a harmonic source, with w being the angular

frequency, e^{-iwt}, the wave equation becomes the Helmholtz equation:

$$\nabla^2 p + k^2 p = 0 \qquad (2.3)$$

with k being the wavenumber. Rewriting the wavenumber k as

$$k = \frac{w}{c} = \frac{w}{c_0}\frac{c_0}{c} = k_0 n \qquad (2.4)$$

where c_0 is a constant reference sound-speed and

$$n = \frac{c_0}{c} \qquad (2.5)$$

is the index of refraction. I write acoustic pressure in the form

$$p = Ae^{ik_0 S(x,y,z)} \qquad (2.6)$$

where A is the wave amplitude, a function of (x,y,z), and $k_0 S$ is the phase of the wave. Substituting equation (2.6) into equation (2.3), and collecting together the real and imaginary parts results in the equations

$$\nabla^2 A - k_0^2 A[n^2 - (\nabla S)^2] = 0 \qquad (2.7)$$

and

$$2\nabla A \cdot \nabla S + A\nabla^2 S = 0 \qquad (2.8)$$

If we make the assumption:

$$\left|\frac{\nabla^2 A}{k^2 A}\right| \ll 1 \qquad (2.9)$$

then this implies the rate of variation of the wave phase, per wavelength, of the vertical component of wavelength is small (Tolstoy and Clay, 1966). Equation (2.10) can be shown to follow from equation (2.9) (Frisk, 1991)

$$\left|\frac{dc}{dz}\right| \ll \frac{c}{\lambda} \qquad \textbf{(2.10)}$$

where λ is the wavelength. This is a necessary, but not sufficient, condition for the ray acoustics approximation. It is also necessary that the reference point is not in the shadow zone or near its boundaries, and also not near caustics (Brekhovskikh and Lysanov, 1982). Even simpler, the medium must vary slowly over an acoustic wavelength. This is the geometric approximation.

Applying the condition (2.9) to equation (2.7), results in:

$$(\nabla S)^2 = n^2 \qquad \textbf{(2.11)}$$

or, expanding the gradient operator:

$$\left(\frac{\partial S}{\partial x}\right)^2 + \left(\frac{\partial S}{\partial y}\right)^2 + \left(\frac{\partial S}{\partial z}\right)^2 = n^2 \qquad \textbf{(2.12)}$$

This is the eikonal equation, which forms the basis for ray theory. A physical picture of rays follows directly from the eikonal equation. Surfaces of constant phase (wave fronts) are given by S = constant, and the lines orthogonal to the wave fronts (∇S) define the geometry of the rays(Brekhovskikh and Lysanov, 1982). The rays represent the paths along which acoustic energy propagates. The amplitude of the rays is given by equation (2.8), the transport equation. For our purposes, we

consider propagation in the vertical plane and let sound-speed be a function of depth only (i.e., c = c(z)) between sound-speed profile segments; a good approximation because of the vertically stratified nature of the ocean. Thus, if an acoustic signal has a wavelength that is much less than the length scale being examined then the geometric approximation is valid and ray theory can be used to model the acoustic field.

In middle latitudes the sound-speed decreases from the surface to a minimum axis at ~1000m due to temperature decreasing, and then increases to the bottom due to pressure increasing in the nearly isothermal depths of the ocean(Fig 2.2).

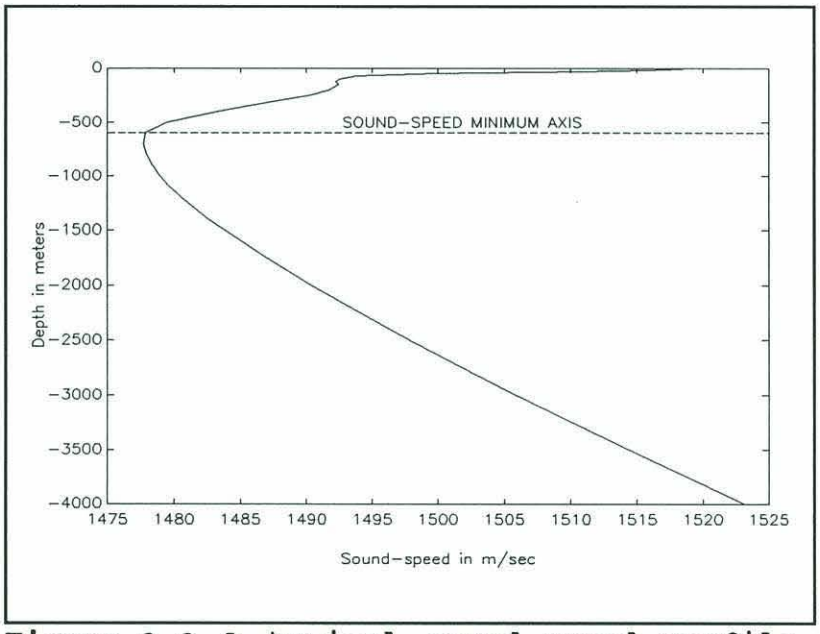

Figure 2.2 A typical sound-speed profile. Sound-speed is computed with Del Grosso's alg. using Levitus data (Levitus, 1982).

Sound rays bend towards minimum sound speed according to Snell's law of refraction

$$\frac{\cos\theta_1}{c_1} = \frac{\cos\theta_2}{c_2} = Constant \qquad (2.13)$$

where c_i is sound-speed in the layer and θ_i is the angle the ray makes with the horizontal.

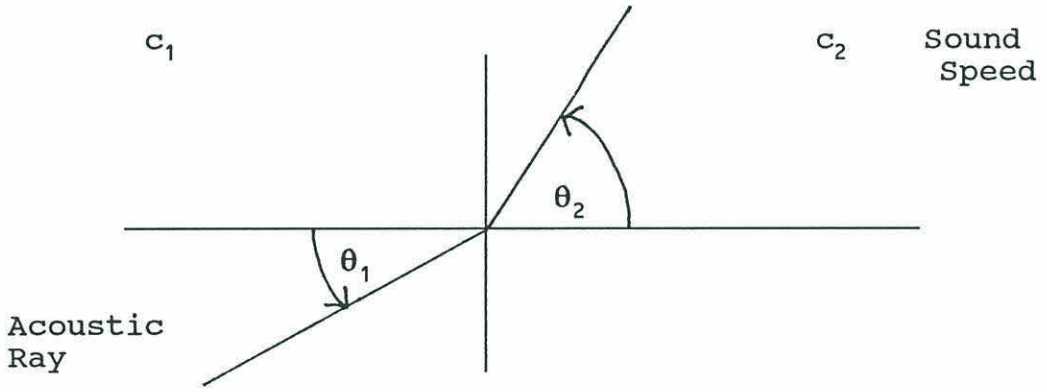

Figure 2.3 Snell's law of refraction for $c_1 < c_2$.

This shows that sound rays will constantly refract toward the area of lower sound-speed. Because there is a minimum in sound-speed, at about 1 km depth at mid-equatorial latitudes, sound energy is bent away from the high loss regions of the surface and bottom. Each ray path samples a different vertical section of the ocean depending on the launch(departure) angle from the source. Travel times for ray paths are different because sound speeds are different along their paths. These times are given by

$$T = \int_p \frac{ds}{c(s)} \qquad (2.14)$$

where T is the travel time along the ray path for a particular ray, p is the ray path, ds is the arc length, and c(s) is the sound-speed at each point along the path. The ray paths are such that only a few rays actually connect the source and the receiver; these are defined as eigen-rays.

2.3 The Ray Tracing Program

In this project, we used the range dependent ray tracing program MPP (Multiple Profile ray tracing Program) developed by C. W. Spofford. The sound-speed field is linearly interpolated in both depth and range in specified triangular sectors. The sound-speed field is continuous everywhere, but is's gradient is discontinuous at the triangular boundaries. The bottom bathymetry is represented by piece-wise linear segments. Output of the program includes eigen-ray arrival times and transmission loss (calculated from geometrical spreading and losses due to boundary reflections), along with a history of the eigen-ray trajectories.

The geodesic path between the source and receiver was computed using the WGS84 reference ellipsoid of the Earth (Defense Mapping Agency, 1987). We compute sound speed profiles from the Levitus seasonal data base(Levitus, 1982) using Del

Grosso's algorithm (equation. 2.1). Bathymetry points along the geodesic are from a digital data base (National Geophysical Data Center, 1987). Using a flat-Earth coordinate transformation (Ben-Menahem and Sarva, 1981), rays are traced in a Cartesian coordinate system.

MPP computes two types of rays (Spiesberger et al., 1991). The first type, the geometric ray, passes through both the source and receiver. The second type, the diffracted arrival (Brown, 1982; Pierce, 1981), does not pass through the receiver, but through points near the receiver. Because propagation is at finite frequency, energy leaks into the receiver by diffraction as an exponentially decreasing wave.

2.4 Linearizing The Forward Problem

The travel-time of the i_{th} ray along path Γ_i is given by

$$T_i = \int_{\Gamma_i} \frac{ds}{c(s) + u \circ \tau} \qquad (2.15)$$

where ds is a differential arc-length along the path Γ_i, c(s) is the sound-speed, u is the current component along the ray, $\circ$ is a dot product, and τ is a unit vector tangent to the ray. The travel time of a given ray is dependent upon the path length, sound-speed, and current velocity along the ray path. Variations in sound-speed and current will lead to deviations in travel-time and a change in the ray path. Hamilton et al., (1980) showed that there is a small change in travel-time associated with this change in path length if sound speed and current variations are small. However, the change in path length leads to a different sampling of the oceanic medium.

Now we will examine the relative size of the terms in the denominator of the integrand of equation (2.15). A typical value for current speed is u = 0.1 m/s and a typical sound-speed is c = 1500 m/s, so $\left|\frac{u}{c}\right| = O(10^{-4}) \ll 1$.

Typical values for the vertical shear of current and sound speed are $\frac{du}{dz} = \frac{0.1 m/s}{100 m} = O(10^{-3})$ and $\frac{dc}{dz} = \frac{5 m/s}{100 m} = O(10^{-2})$, so $\frac{dc}{dz}$ is usually one order of magnitude larger than $\frac{du}{dz}$. The refraction of rays is dominated by the sound-speed gradient, and the current can be ignored in ray tracing, to first

order.

The path of the ray in equation(2.15) is a nonlinear function of the sound-speed field, so we linearize about a reference state, c_0, as in:

$$c(\chi) = c_o(\chi) + \delta c(\chi) \qquad \textbf{(2.16)}$$

where δc is the perturbation from the reference field. Also

$$|\delta c(\chi)| \ll c_o(\chi) \qquad \textbf{(2.17)}$$

Substituting (2.16) into the travel-time integral (2.15) gives

$$T_i = \int_{\Gamma_i} \frac{dS}{c_o(S) + \delta c(S) + u \cdot \tau} \ . \qquad \textbf{(2.18)}$$

Expanding the integrand, keeping only the leading order terms, and dropping the current velocity term yields:

$$T_i \approx \int_{\Gamma_i} \frac{dS}{c_o(S)} - \int_{\Gamma_i} \frac{\delta c(S)\ dS}{c_o^2(S)} \ . \qquad \textbf{(2.19)}$$

Thus the travel-time perturbation can be expressed as

$$\delta T_i \approx - \int_{\Gamma_i} \frac{\delta c(S)\ dS}{c_o^2(S)} \ . \qquad \textbf{(2.20)}$$

Equation (2.20) is linear in the sound-speed perturbation, δc, if Γ_i is assumed not to change as the sound-speed field perturbs. The forward problem is finding the δT_i when δc is known.

Sound-speed is directly proportional to temperature (θ),

with an empirical relationship given by: (Del Grosso, 1974)

$$\frac{\delta C}{C_o} = \alpha \delta\theta \qquad (2.21)$$

where $\alpha = 3.2 \times 10^{-3}$. Thus equation (2.20) can be considered a linear relationship between the travel-time perturbations and perturbations in temperature.

2.5 Identification of Eigen-rays

To identify eigen-rays for the spring and summer seasons I computed a daily average of the 12 arrival records for each day data was available as prescribed by Spiesberger et al., (1980). I compared the output of MPP for spring and summer seasons to the daily averages. The output of the MPP ray tracing program is shown in Figures 2.4a and 2.5a. The Levitus data base for the spring and summer seasons is used to generate sound speed profiles with Del Grosso's algorithm(equation. 2.1). The Levitus data base is divided into the four seasons according to Table 2.1.

Table 2.1 Levitus data base seasons

Season	Calendar Months	Calendar Days
Spring	May - June	121 - 212
Summer	August - October	213 - 304
Winter	November - January	305 - 031
Fall	February - April	032 - 120

Daily averages for Days 189 and 257 are shown in Figures 2.4b and 2.5b. Six eigen-rays (all geometric ray arrivals) were identified for the spring season. The last pair of arrivals, in Figure 2.4b, are predicted as diffracted arrivals from MPP output. Because there are a large number of diffracted rays from MPP output grouped together near the peak arrival time, the individual diffracted rays could not be resolved with 16 ms resolution. The individual rays of the groups near the last two arrivals have different paths, sampling different parts of the ocean and thus are not used here for tomographic inversions.

For the summer season seven geometric eigen-rays were identified. The last arrival was predicted from MPP as a diffracted arrival and the individual diffracted rays could not be resolved. The geometric rays that have larger travel times than the identified eigen-rays intersect the bottom at large angles and are not observed at the receiver.

The daily average for day 189 is compared with the MPP spring

ray trace output in Figure 2.6a. Figure 2.6b shows the daily average for day 257 compared to the MPP spring ray trace output.

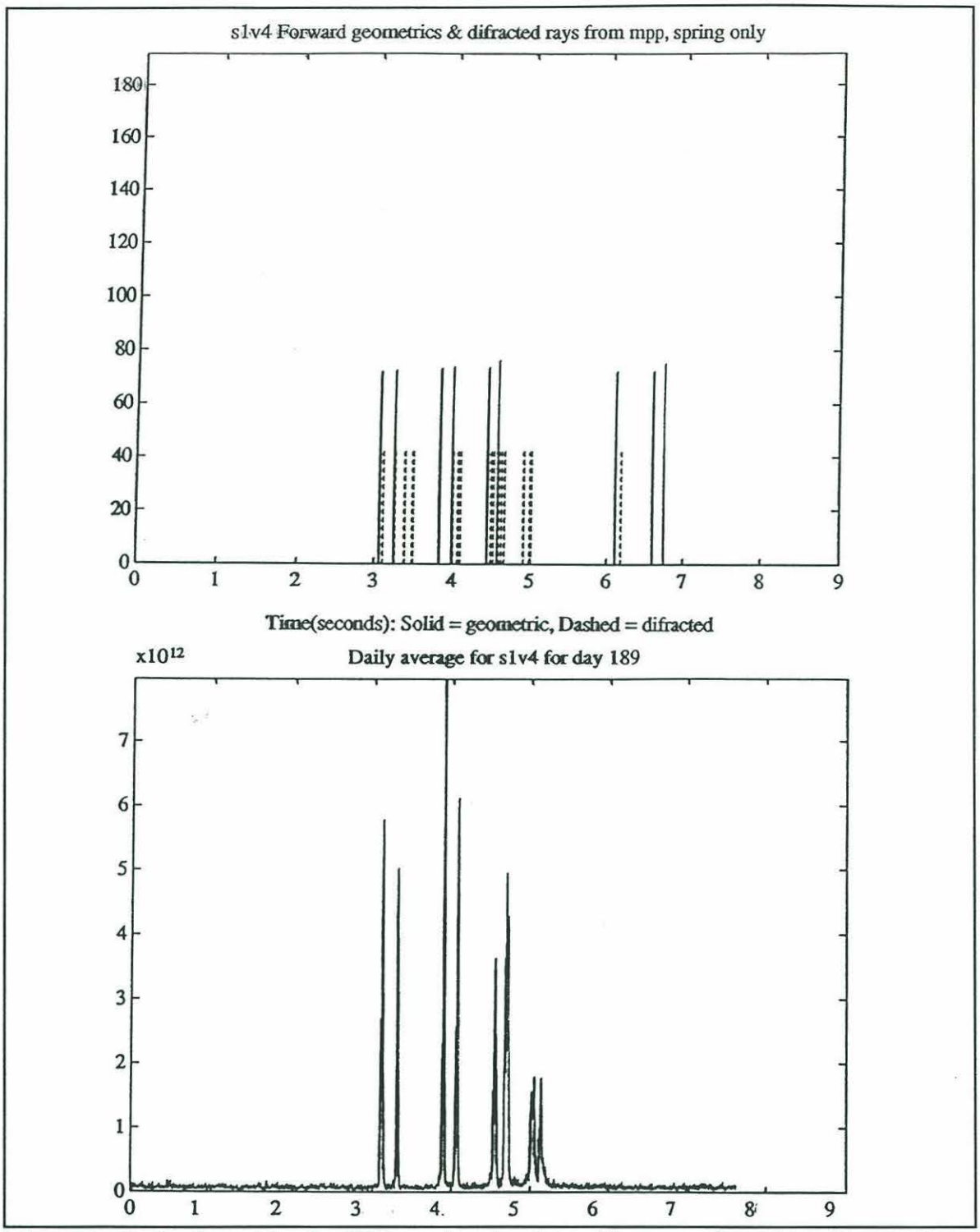

Figure 2.4 (a. Top) MPP output for the spring Levitus data base. **(b. Bottom)** Daily average for julian day 189. X-axis is time(s), Y_axis is relative magnitude and the start time is about 20 minutes.

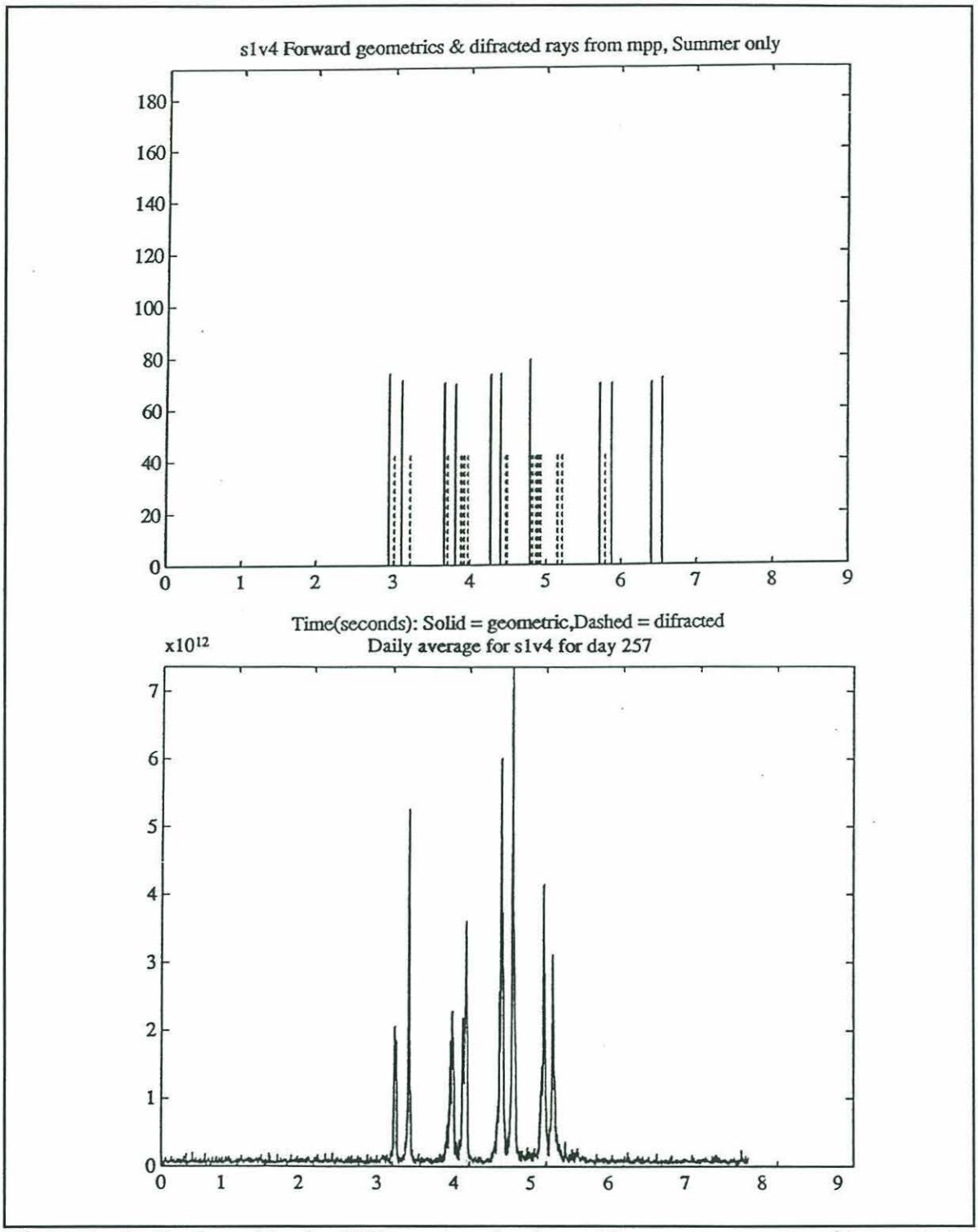

Figure 2.5 (a. Top) MPP output for the summer Levitus data base. **(b. Bottom)** Daily average for julian day 257. The X-axis is time(s), the Y-axis is relative magnitude, and the start time is about 20 minutes.

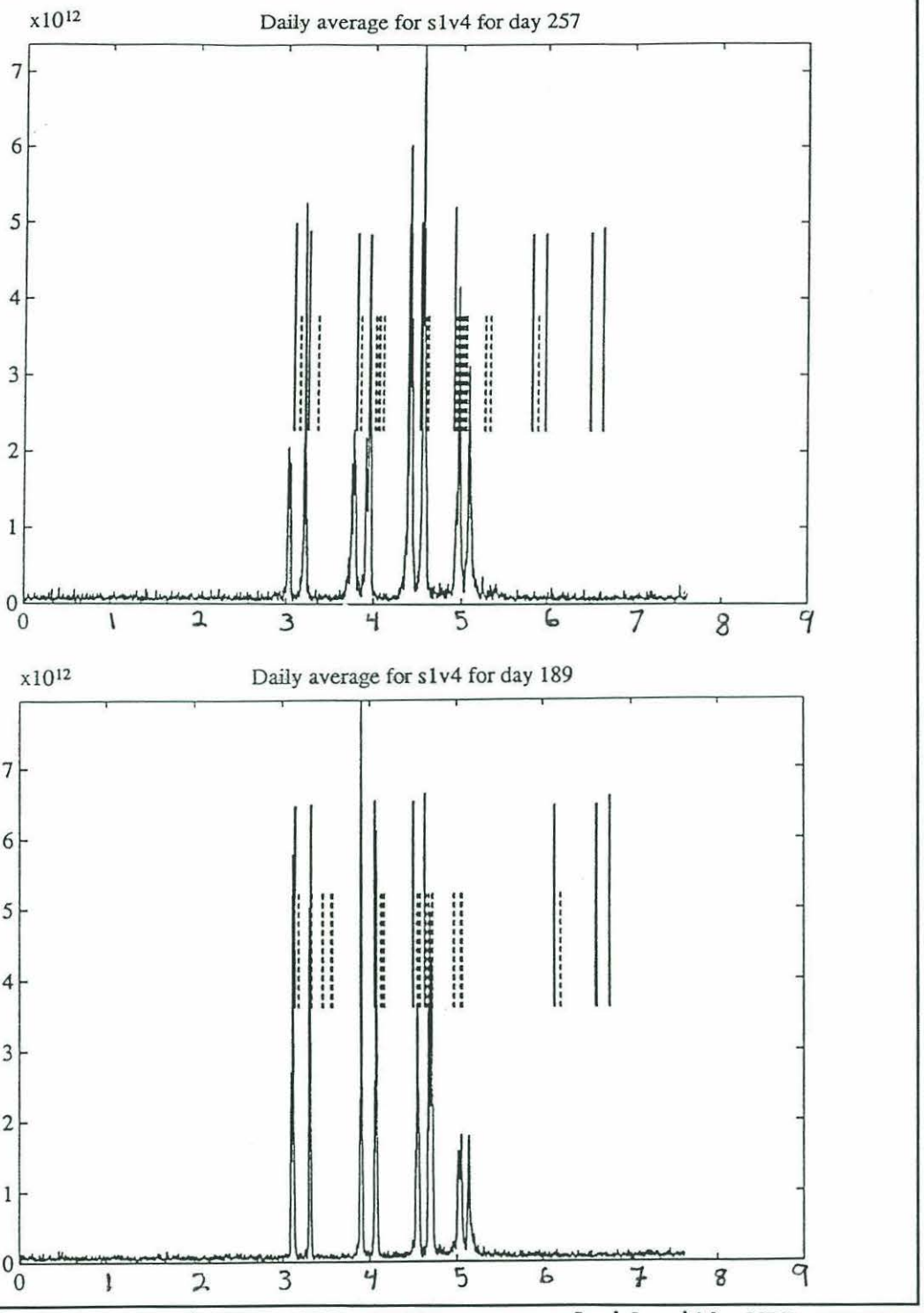

Figure 2.6 (a. Top) Day 257 average overlaid with MPP summer output **(b. Bottom)** Day 189 average and MPP spring output. The X-axis is time(s) and the Y_axis is relative magnitude. The MPP output was shifted 60ms.

Table 2.2 shows the difference in travel time (ms) between the observed daily average peak arrival time for days 189 and 257 and the predicted eigen-ray travel time for the spring and summer seasons respectfully. Predicted times were less than their corresponding observed arrival times for all rays (Table 2.2). A time difference of 0.1 second between measured and predicted travel times in the upper 1000m along our ray paths equates to less than 0.1°C temperature difference (Spiesberger et al., 1983).

Table 2.2 Daily average peak arrival time (measured) - ray travel time (predicted); for days 189 and 257, Spring and Summer.

Peak/Ray	Spring travel time difference(ms) measured - predicted	Summer travel time difference(ms) measured - predicted
1	60	90
2	75	97
3	70	101
4	80	118
5	118	130
6	133	156
7	Not Applicable	159

2.6 Variations in the Forward Model

I ran the MPP ray tracing program for the four seasons using the Levitus climatological data base of the oceans to compute sound speed profiles with Del Grosso's algorithm (equation. 2.1). We identified six eigen-rays (all geometric arrivals) for the spring, fall, and winter seasons and seven for the summer season. The first 100 km of the propagation path of the six eigen-rays common to all four seasons are shown in Figure 2.7(a-f).

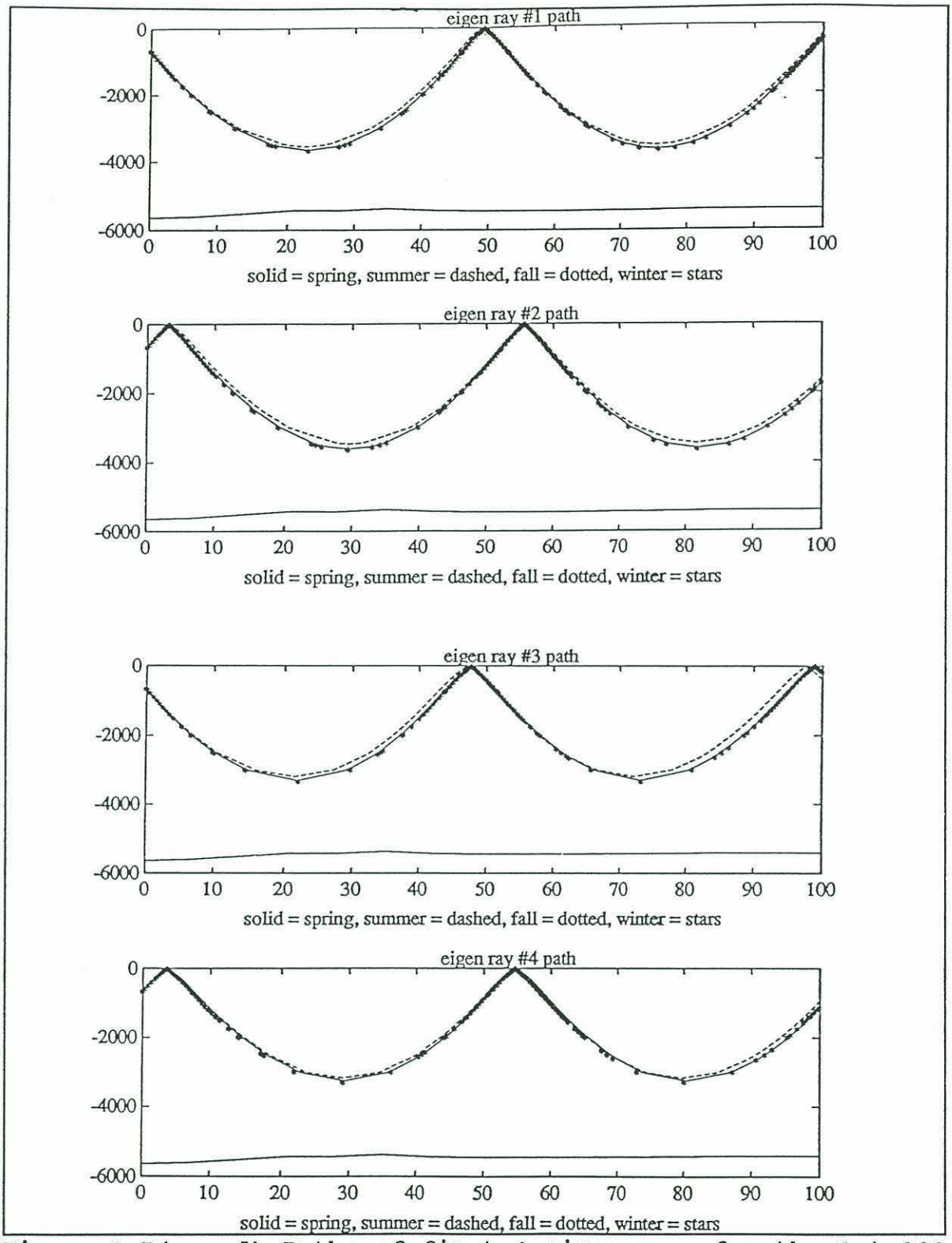

Figure 2.7(a - d) Paths of first 4 eigen rays for the 1st 100 km. X-axis is horizontal range(km) and the Y_axis is depth(m).

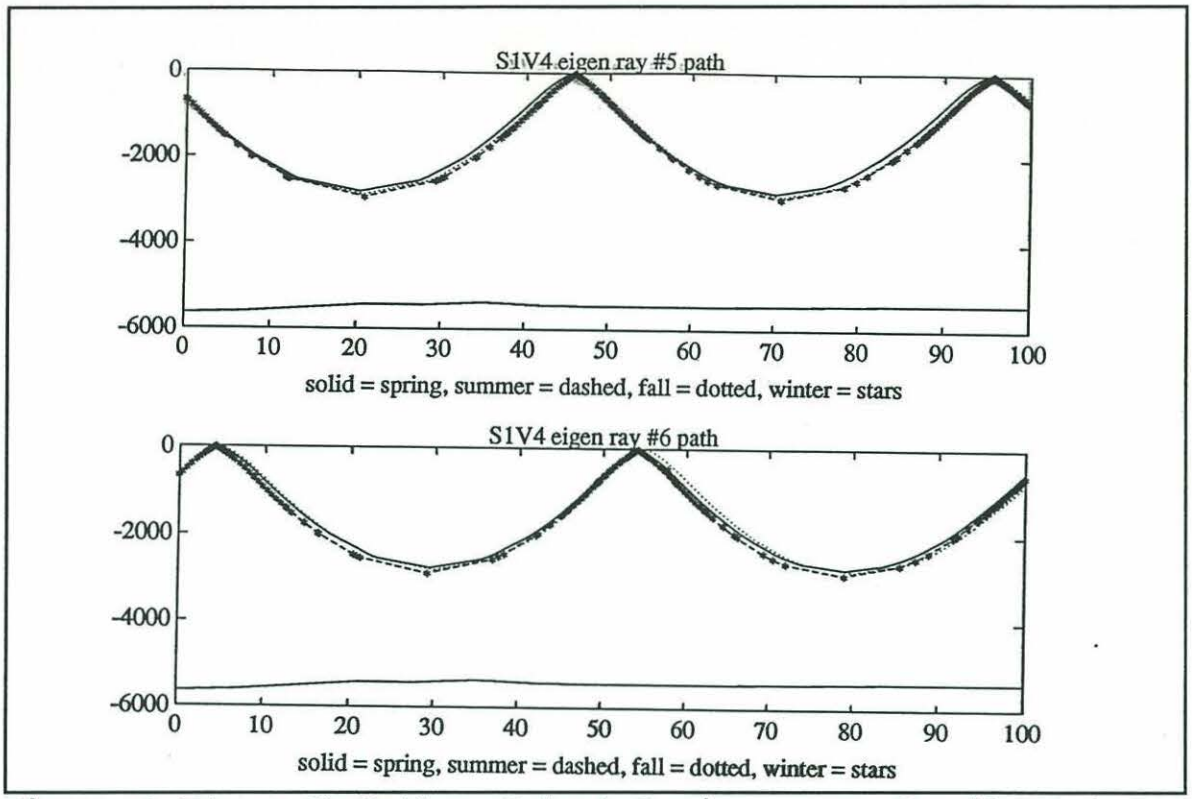

Figure 2.7(e - f) Paths of last 2 eigen rays for the 1st 100 km. The X-axis is horizontal range(km) and the Y-axis is depth(m)

To compare the nonlinearity of the forward problem for the four seasons we follow in a similar fashion to a derivation found in Spiesberger (1985). The reference travel time between a fixed source and receiver along the reference ray path Γ_0 is given by:

$$T_0 = \int_{\Gamma_0} \frac{dS}{c_0} \qquad (2.22)$$

where $c_0 = c_0(x,z)$ is the initial sound speed. The perturbed travel time along the perturbed ray path Γ_1 is given by:

$$T_1 = \int_{\Gamma_1} \frac{dS}{c_0 + \delta c} \qquad (2.23)$$

where $\delta c = \delta c(x,z)$ is the perturbation in the sound speed. The perturbed ray path becomes the unperturbed ray path as $\delta c \to 0$. The change in travel time between the initial and perturbed state is given by:

$$\delta T_1 = T_1 - T_0 = \int_{\Gamma_1} \frac{dS}{c_0 + \delta c} - \int_{\Gamma_0} \frac{dS}{c_0} \, . \qquad (2.24)$$

Because $|\delta c/c_0| \approx .003$ for mid-ocean sound speed perturbations we can expand T_1 as:

$$T_1 = \int_{\Gamma_1} \frac{dS}{c_0 + \delta c} = \int_{\Gamma_1} \frac{dS}{c_0}\left[1 - \frac{\delta c}{c_0} + \left(\frac{\delta c}{c_0}\right)^2 - \cdots\right] . \qquad (2.25)$$

Thus δT_1 becomes:

$$\delta T_1 = \int_{\Gamma_1} \frac{dS}{c_0}\left[1 - \frac{\delta c}{c_0} + \left(\frac{\delta c}{c_0}\right)^2 - \cdots\right] - \int_{\Gamma_0} \frac{dS}{c_0} \qquad (2.26)$$

or

$$\delta T_1 = \left(\int_{\Gamma_1} \frac{dS}{c_0} - \int_{\Gamma_0} \frac{dS}{c_0}\right) - \int_{\Gamma_1} dS \left[\frac{\delta c}{c_0^2} - \frac{\delta c^2}{c_0^3} + \cdots\right] . \qquad (2.27)$$

This can be written as:

$$\delta T_1 = \left(\int_{\Gamma_1} \frac{dS}{c_0} - \int_{\Gamma_0} \frac{dS}{c_0}\right) - \int_{\Gamma_1} dS \, \frac{\delta c}{c_0^2}\left[1 - \frac{\delta c}{c_0} + \cdots\right] \qquad (2.28)$$

the last term of equation (2.28) can be written as

$$-\int_{\Gamma_1} dS\ \frac{\delta c}{c_0^2}\left[1 - \frac{\delta c}{c_0} + \cdots\right] = -\int_{\Gamma_0} dS \frac{\delta c}{c_0^2} + \delta T_4 \quad . \qquad (2.29)$$

The first term of on the right-hand-side of equation (2.29),

$$\delta T_2 = -\int_{\Gamma_0} dS \frac{\delta c}{c_0^2} \qquad (2.30)$$

is a linear approximation for the exact travel time change. The most important part of the linearizing is that $\Gamma_1 = \Gamma_0$ (i.e. the perturbed path is the same as the reference path).

Defining

$$\delta T_3 = \int_{\Gamma_1} \frac{dS}{c_0} - \int_{\Gamma_0} \frac{dS}{c_0} \qquad (2.31)$$

and writing δT_4 from equation (2.29) as

$$\delta T_4 = \int_{\Gamma_0} dS \frac{\delta c}{c_0^2} - \int_{\Gamma_1} dS \frac{\delta c}{c_0^2} + \int_{\Gamma_1} \frac{dS\ \delta c^2}{c_0^2 (c_0 + \delta c)} \qquad (2.32)$$

allows the exact travel time change to be written as

$$\delta T_1 = \delta T_2 + \delta T_3 + \delta T_4 \ . \qquad (2.33)$$

This can be expressed as

$$\delta T_1 = T_1 - T_0 = \delta T_2 + NL \qquad (2.34)$$

or

$$NL = (T_1 - T_0) - \delta T_2 \qquad (2.35)$$

where

$$NL = \delta T_3 + \delta T_4 \ . \qquad (2.36)$$

NL contains all of the nonlinear terms of the forward problem. If the initial ray and the perturbed ray coincide everywhere then NL = 0. The percentage of nonlinearity of the forward problem is:

$$\%NL = 100\left(\frac{NL}{\delta T_1}\right) \ . \qquad (2.37)$$

%NL is a measure of the nonlinear effects, primarily due to changes in the ray path, it is a measure of the errors of the linear approximation δT_2 verses the exact travel time change δT_1.

For our experiment we used the Levitus summer sound speed profiles and the MPP output ray paths as our reference state and the other seasons as our perturbed states. T_0 and T_1, the travel times along the reference and perturbed paths are obtained from MPP output. %NL was computed using the summer as reference for all six of the eigen-rays for each of the other seasons. The results are summarized in Table 2.3.

Most of the rays have large nonlinearity, thus δT_2 is not a good approximation to the exact travel time changes for these rays. There are exceptions; for example eigen-ray # 3 for two seasons and eigen-ray # 4 for all seasons have small nonlinearity.

Table 2.3 Seasonal variations in the forward model. δT_1 is given by Eq. 2.24, δT_2 by Eq. 2.30, NL by Eq.2.35 and %NL is given by Eq. 2.37. The reference paths are computed from the summer time values.

Season	δT_1(s)	δT_2(s)	NL(s)	%NL
Eigen ray # 1				
Spring	.125	.170	-.045	-35.8
Fall	.120	.196	-.076	-63.6
Winter	.174	.309	-.135	-77.1
Eigen ray # 2				
Spring	.139	.195	-.054	-39.7
Fall	.133	.231	-.098	-73.4
Winter	.192	.362	-.170	-88.7
Eigen ray # 3				
Spring	.176	.193	-.017	-10.0
Fall	.171	.203	-.032	-18.3
Winter	.237	.351	-.114	-47.9
Eigen ray # 4				
Spring	.188	.174	.014	7.39
Fall	.185	.171	.014	7.42
Winter	.255	.301	-.046	-17.98
Eigen ray # 5				
Spring	.174	.110	.064	36.4
Fall	.188	.068	.120	63.4
Winter	.276	.147	.129	46.6
Eigen ray # 6				
Spring	.171	.110	.061	35.6
Fall	.190	.064	.126	66.3
Winter	.286	.142	.144	50.4

Table 2.4 shows the first upper turning depths for the six eigen-rays for each season.

Table 2.4: Eigen ray upper turning depth for the four seasons.

First upper turning point (m)						
Ray #	1	2	3	4	5	6
Spring	0	0	0	0	18.5	23.1
Summer	16.6	22.1	30.9	32.2	38.9	40.8
Fall	0	0	0	0	0	0
Winter	0	0	0	0	0	0

2.7 Observational Variations in Travel Time

Figure 2.8a is a gray scale bit plot of the observed data with the darker shades corresponding to stronger amplitudes. Peaks (arrivals) were picked from the data using a variable size window scheme that determined the largest signal within the window. The picked peaks are shown in white in Figure 2.8b. The daily average multipath arrival (peaks) trends are shown in Figure 2.9. Variations in the travel time of the daily averages are larger for the later arrivals than the early arrivals. Multipath arrivals start arriving earlier around year day 180 (late June) with the sharpest decrease in arrival times between late June and late July. The later arrivals correspond to rays with smaller launch angles, thus sampling less of the deep and surface water.

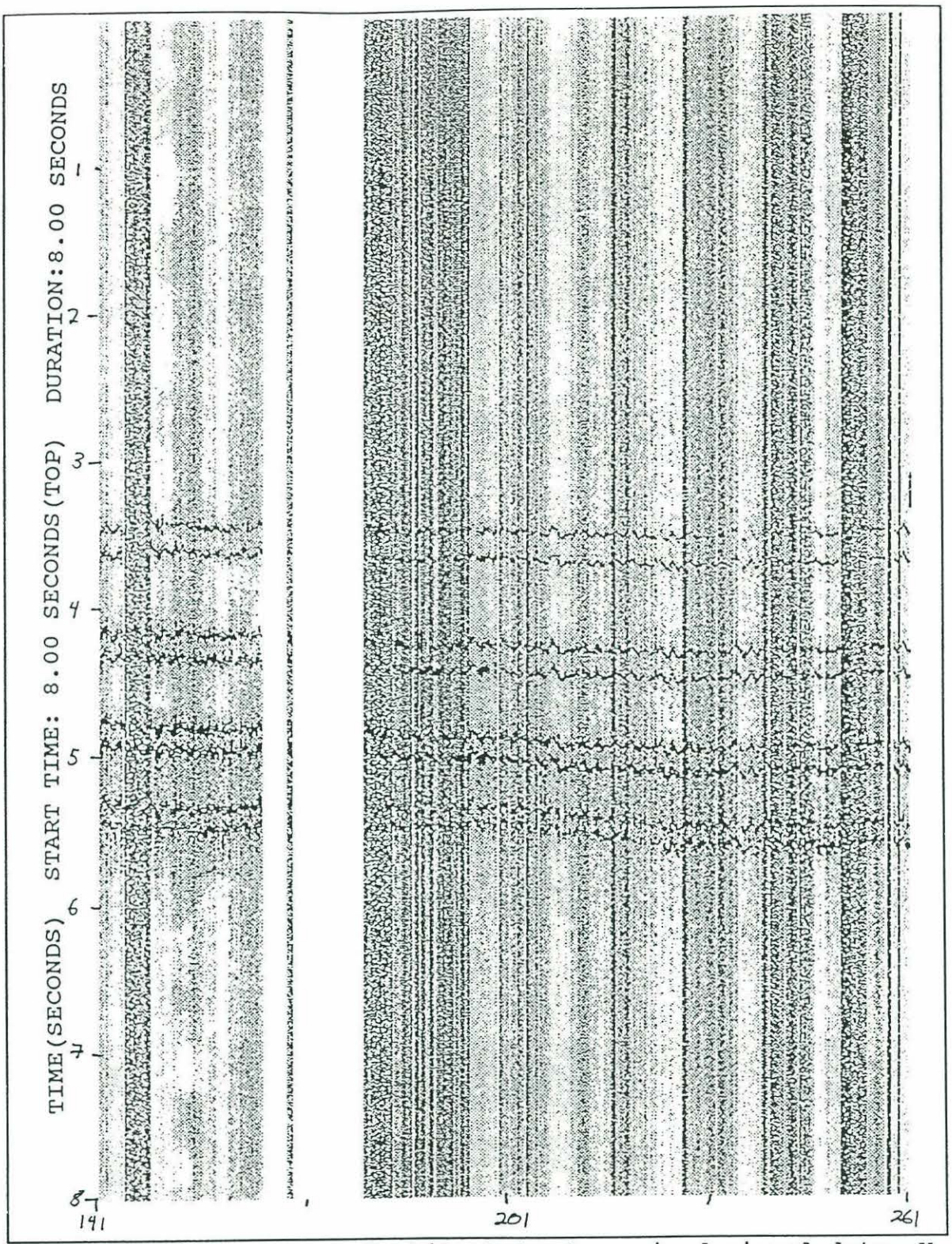

Figure 2.8 (a.) Gray scale bit plot of received signal data. X-axis is yearday. Starting 141 and ending 261. Y-axis is time(s)

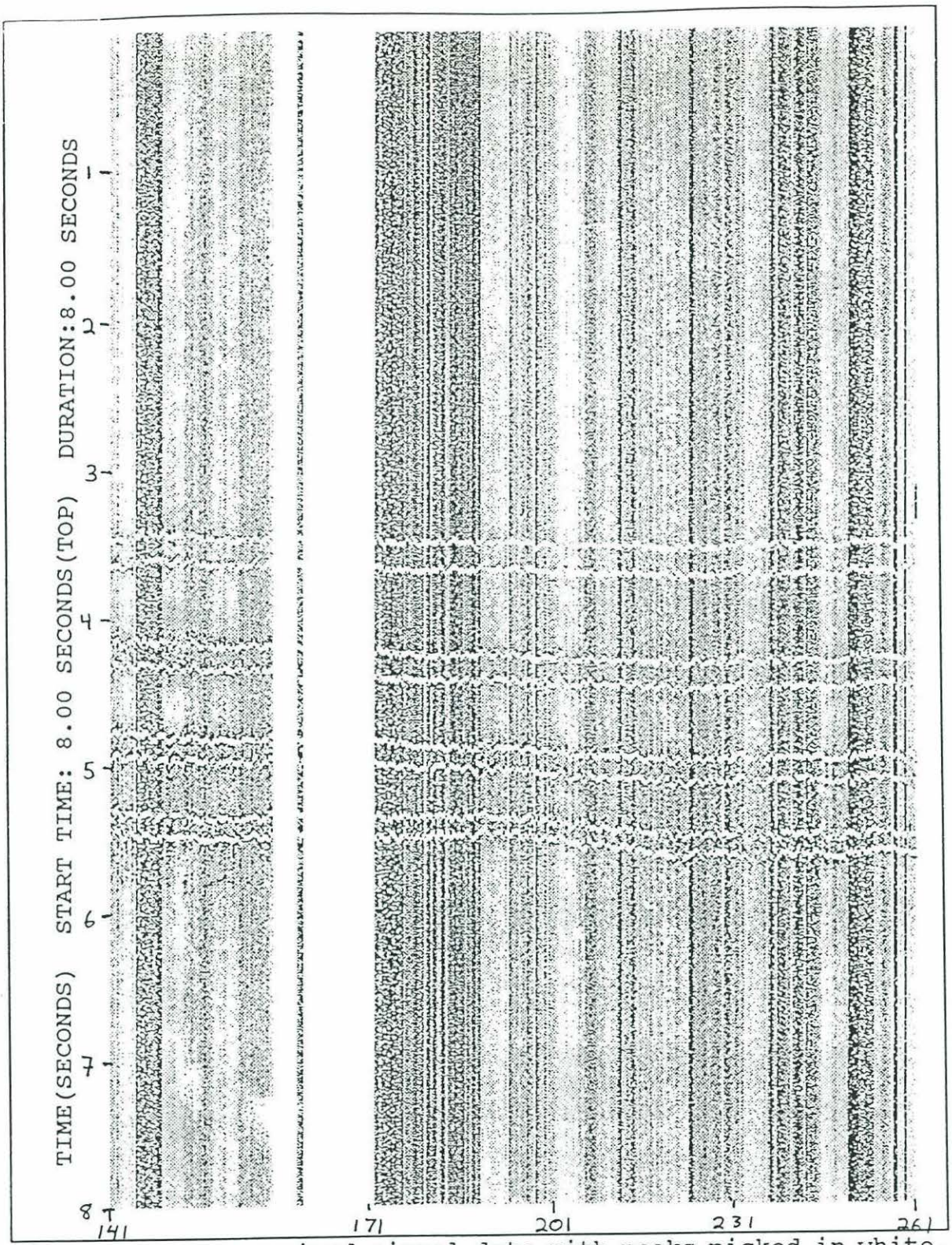

Figure 2.8 (b) Received signal data with peaks picked in white. X-axis is yearday and the y-axis is time(s)

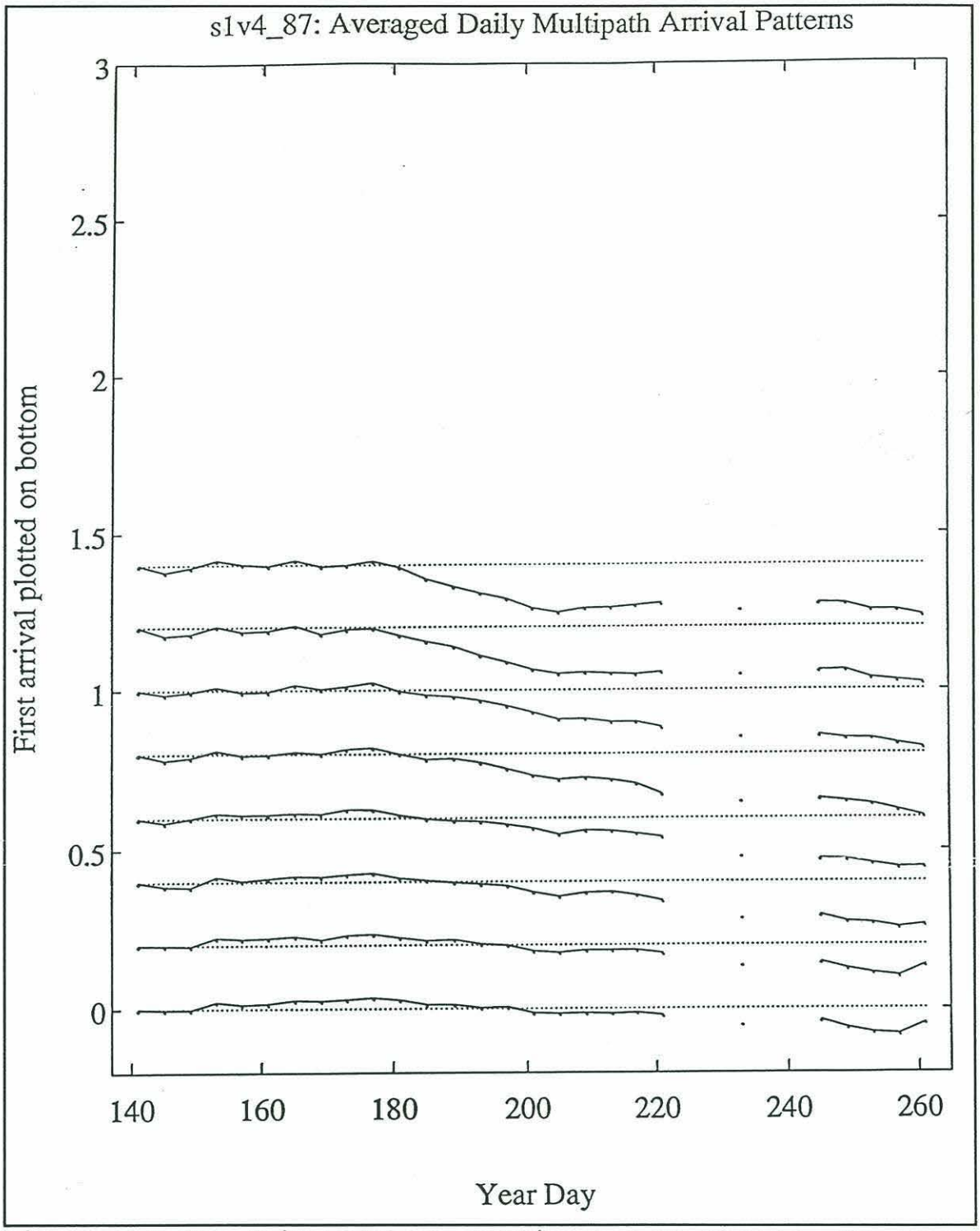

Figure 2.9 The daily average multipath peak trends. The start times of the trends are offset by 0.2 s and initialize to zero at day 140. The Y-axis is in seconds and the X-axis is 1987 yeardays.

Chapter III

Surface Solar Irradiance Variations

3.1 Satellite Data

The four components of the surface heat flux budget are: 1) the net surface short wave radiation; 2) the net surface long wave radiation; 3) sensible heat; and 4) latent heat. Chertock (1989) generated a global seven year record of net solar irradiance at the ocean surface for the period between November 1978 and October 1985. Her algorithm is based on a radiative transfer theory. Surface solar irradiance is the net radiation from the sun entering the surface of the ocean. The surface solar irradiance was computed by subtracting the sum of solar energy absorbed by the atmosphere plus the solar energy reflected by the ocean-atmosphere system from the solar energy at the top of the atmosphere.

The solar energy absorbed by the atmosphere is a modeled quantity computed by Chertock (1989). Albedo is the ratio of the radiation reflected by a body to the amount incident upon it. Planetary albedo is measured by satellite for this experiment. The solar energy at the top of the atmosphere is a known quantity calculated according to the astronomical sun-earth geometry.

The planetary albedo used as input for Chertock's algorithm came from the Nimbus-7 satellite. The Earth Radiation Budget

(ERB) experiments Wide Field Of View (WFOV) radiometer on Nimbus-7 provided the measurements (NASA, 1984b). Twenty-two spectral channels of radiation were measured by the ERB experiment instruments. The infrared radiation emitted by the earth and the solar radiation reflected by the earth are measured by the four fixed sensors of the WFOV radiometer part of the ERB package. The footprint (ground resolution) of the WFOV instrument aboard Nimbus-7 is approximately 1000km (NASA, 1984a). The WFOV radiometer measures the reflected solar radiation in the spectral range between 0.2 and 3.8μm (NASA, 1984b).

The Nimbus-7 satellite was launched on October 24, 1978 into a nearly circular, sun-synchronous orbit at an altitude of 950km. The sun-synchronous orbit provides two passes per day, near local noon and midnight for equatorial crossings. Measurements by a satellite in a sun-synchronous orbit are always made at the same times for a given location (Stewart, 1985). This produces a biased distribution of data over the diurnal cycle. If the parameter being measured varies diurnally, as planetary albedo does, the bias must be accounted for in the computations.

The diurnal variations in the albedo are quite large, a factor of 1.5 to 2 for clouds and a factor of 4 for ocean surfaces (Hucek et al., 1987). There are also diurnal variations in cloud cover (Minnis and Harrison, 1984) that add to the diurnal variability of the albedo.

Albert Arking of the Goddard Space Flight Center designed a global reflectance model to convert the measured WFOV planetary albedo to a daily average planetary albedo. He used the Nimbus-3 directional reflectance models designed by Raschke et al.(1973) to estimate that 90% of the solar radiation reflected came from cloud-land reflectance and about 10% was from ocean reflectance (Kyle et al., 1986). Table 3.1 shows the Nimbus-3 directional values derived by Raschke et al., (1973) and the Nimbus-7 ERB WFOV composite-directional reflectance model.

Table 3.1 Normalized directional reflectance used in Nimbus-7 ERB algorithms to calculate planetary albedo diurnal correction factors (Kyle et al., 1986)

Cosine of solar zenith angle	Ocean	Cloud/ land	WFOV Composite*
0.95	1.00	1.00	1.00
0.85	1.00	1.00	1.00
0.75	1.04	1.09	1.09
0.65	1.17	1.18	1.18
0.55	1.43	1.28	1.30
0.45	1.78	1.37	1.41
0.35	2.24	1.47	1.55
0.25	2.79	1.56	1.68
0.15	3.40	1.60	1.78
0.05	4.00	1.60	1.84

* Composite is 90% cloud/land plus 10% ocean.

The planetary albedo data was processed using calibration adjustment procedures detailed in Kyle et al.(1985). Daily mean planetary albedo data is computed (Kyle et al., 1986) from the

instantaneous measurements of the Nimbus-7 ERB experiment.

To use the computed daily average planetary albedo for studies of the global radiation budget it is necessary to weight the measured solar flux by the daily average insolation at the top of the atmosphere (Hucek et al., 1987). $\bar{A}_{sat}$, the monthly mean planetary albedo, is computed from

$$\bar{A}_{sat} = \frac{\sum_{i=1}^{M} k_i \bar{F}(\phi, \lambda, t_i)}{\sum_{i=1}^{M} \bar{F}_{MAX}(\phi, \lambda, t_i)} \qquad (3.1)$$

Where M is the number of days in the month and k_i is the albedo normalization constant for the i_{th} day. F is the instantaneous calibrated measurement of the reflected solar radiation. F_{MAX} is the amount of solar radiation that would have been reflected by the incident object if it had a perfectly reflecting diffuse surface. $\bar{F}$ and $\bar{F}_{MAX}$ are the average of F and F_{MAX} for all the measurements within the field of view for a single pass of the satellite. ϕ is the latitude of the sub-point target area, λ is the longitude of the sub-point target area, and t_i is the day of the year.

3.2 Computation of Surface Solar Irradiance

The solar irradiance at the ocean surface was computed by Chertock using her algorithm based on radiative transfer theory (Chertock, 1989; Frouin and Chertock, 1992; Chertock et al., 1992). Chertock developed a layered model of the atmosphere based on plane-parallel theory to compute surface solar irradiance. The top layer is a clear sky atmosphere which is above, and decoupled from, an effective cloud layer. The solar irradiance at the surface is a result of the radiation passing through the clear sky and cloud layers. The solar radiation incident at the top of the atmosphere is reduced by scattering and absorption through the clear sky layer by aerosols and molecules. The solar radiation is further reduced as it passes through the cloud layer by absorption and multiple reflections. Chertock used this algorithm (Chertock, 1989; Frouin and Chertock, 1992) to convert the monthly mean planetary albedo data provided by the satellite to surface solar irradiance.

The largest contributors to atmospheric absorption of radiation in the solar spectrum are oxygen (O_2), carbon dioxide (CO_2), ozone (O_3), and water vapor (H_2O) (Wallace and Hobbs, 1977). The first two, O_2 and CO_2, are well mixed in the atmosphere and can be considered to be at constant concentrations for radiation study purposes. However, the concentration and distribution of ozone and water vapor are highly variable, both in time and space, thus having a variable effect on the amount

of reflected radiation measured by satellite (Wallace and Hobbs, 1977).

Chertock used the algorithm created by Tanré et al.,(1986) to compute atmospheric absorption and scattering in the clear sky layer. This code, referred to as "5S" (Simulation of the Satellite Signal in the Solar Spectrum), relates the radiative properties of the planetary system to the satellite measured solar radiance in clear atmosphere. The "5S" code was used to compute the diffuse atmospheric transmittance due to scattering by aerosols and molecules. The "5S" code also calculated the transmittance due to gaseous absorption. The code also computed the portion of the measured flux that is from radiation reflected by the atmosphere and returned to space without ever reaching the cloud layer. The 5S code uses the following inputs: 1) the total water vapor and ozone amounts, and the vertical distributions of the ozone and water vapor; 2) the geometrical conditions; 3) The ground reflectance (a function of wavelength); and 4) an aerosol model specifying maritime or continental background and aerosol concentration (a function of visibility).

3.3 Anomalies of Surface Solar Irradiance

Chertock (1989) produced a seven year (November 1978 - October 1985) record of net solar irradiance at the ocean's surface using a numerical code to implement her algorithm. I provided her with Nimbus-7 ERB WFOV planetary albedo data (obtained from NASA's Climate Data System User Support Office at NASA Goddard Space Flight Center) covering the months of interest for the Pacific experiment. She used these data to compute monthly mean surface solar irradiance values for April 1987 through September 1987. The surface solar irradiance data are on a 9° latitude-longitude spacial grid box over the world's oceans.

Climatological monthly means were computed by averaging the data for the reference period (November 1978 - October 1985) excluding El Niño years (January 1982 - December 1983). Errors in the surface solar irradiance values are estimated to range between 10 and 20 W/m^2 (Chertock et al., 1992). Most of the anomalies shown in Figure 3.1(a-f) are within the error limits and thus are not significantly different from zero. The anomalies of surface solar irradiance were computed by subtracting the climatology value from the monthly value. The variation from the monthly means for the months from April 1987 to September 1987 were computed by Chertock for each grid box in the Pacific experiment area. The values shown on Figures 3.1(a - f) represent averages for the entire nine degree grid box.

APRIL 1987 SURFACE SOLAR IRRADIANCE ANOMALIES (W m^{-2})

49.5°N	6.3	-6.3	1.1	1.3		
40.5°	-14.8	-17.4	-2.5	7.1	4.3	
31.5°	-31.5	-29.3	-5.8	8.6	3.8	
22.5°	1.8	-7.3	2.0	11.3	12.0	-5.5
	166.5°W	157.5°	148.5°	139.5°	130.5°	121.5°

Figure 3.1a April 1987. The X-axis is longitude and the Y-axis is latitude.

MAY 1987 SURFACE SOLAR IRRADIANCE ANOMALIES (W m^{-2})

49.5°N	6.7	-1.9	-14.2	-16.4		
40.5°	-4.7	Source -7.0 S1	- - - - -13.9	- - - - -17.5	Receiver -19.4 R1	
31.5°	-6.3	-22.1	-23.9	-20.8	-19.4	
22.5°	-17.1	-19.9	-23.7	-17.3	1.1	7.3
	166.5°W	157.5°	148.5°	139.5°	130.5°	121.5°

Figure 3.1b May 1987, Acoustic path between S1 and R1 is indicated with a dashed line

JUNE 1987 SURFACE SOLAR IRRADIANCE ANOMALIES (W m^{-2})

49.5°N	-37.6	-39.8	-33.7	-22.7		
40.5°	Source -28.7 S3	-28.4	-23.8	-6.9	-12.0	
31.5°	-1.8	-5.6	-3.8	-4.6	R2 -32.9 Receiver	
22.5°	3.8	-1.5	2.1	12.6	-33.7	-8.6
	166.5°W	157.5°	148.5°	139.5°	130.5°	121.5°

Figure 3.1c June 1987, The acoustic path analyzed by Spiesberger and Metzger (1991) S3 - R2 is indicated with a solid line.

JULY 1987 SURFACE SOLAR IRRADIANCE ANOMALIES (W m^{-2})

49.5°N	-20.1	-9.4	-8.3	-15.9		
40.5°	-26.8	-21.2	-26.4	-20.2	-9.7	
31.5°	-8.5	-4.4	-17.9	-10.6	15.8	
22.5°	9.5	0.5	1.2	-6.3	11.2	-8.0
	166.5°W	157.5°	148.5°	139.5°	130.5°	121.5°

Figure 3.1d July 1987

AUGUST 1987 SURFACE SOLAR IRRADIANCE ANOMALIES (W m^{-2})

49.5°N	-19.7	-8.0	-10.5	-15.6		
40.5°	-35.9	-27.0	-21.8	-24.8	-23.9	
31.5°	-7.6	-20.8	-19.6	-14.2	-23.6	
22.5°	12.6	-3.7	-4.6	-0.9	-11.2	-8.4
	166.5°W	157.5°	148.5°	139.5°	130.5°	121.5°

Figure 3.1e August 1987

SEPTEMBER 1987 SURFACE SOLAR IRRADIANCE ANOMALIES (W m^{-2})

49.5°N	-6.8	-11.0	-11.3	-12.3		
40.5°	-14.3	-22.9	-21.0	-16.7	-7.2	
31.5°	-14.4	-17.7	-21.0	-18.2	-11.6	
22.5°	-22.6	-11.5	-4.8	1.1	-7.2	-10.3
	166.5°W	157.5°	148.5°	139.5°	130.5°	121.5°

Figure 3.1f September 1987

To examine the possible effects of changes in surface solar irradiance on acoustic travel times I will look at heating rates in the upper 100 m as Spiesberger and Metzger (1991) did. I will use a model in which the only parameter affecting the heating rate in the upper 100 m is changes in surface solar irradiance. The model does not consider changes in other heat budget terms (section 1.3) nor does it consider advection.

To look at changes in warming, I first determined the average surface solar irradiance anomaly along the acoustic path during each month of the experiment (the dashed line in Figure 3.1(b)). I also determined it for the acoustic path analyzed by Spiesberger and Metzger (1991) (the solid line in Figure 2.1 and in Figure 3.1(c)). The averages were determined by weighing the value in each grid box by the percentage of the path that went through the grid box. The average monthly surface solar irradiance anomalies along both paths are listed in Table 3.2. Note that the magnitude of the anomalies are primarily within the error limits of the surface solar irradiance data noted previously (10 W/m^2 to 20 W/m^2).

Table 3.2 The average surface solar irradiance anomalies (w/m^2) along the acoustic paths for the sections S1-R1 and S3-R2.

	May	June	July	August	Sept.
S1 - R1	-14.5	-17.8	-19.4	-24.4	-17.2
S3 - R2	-14.2	-21.7	-21.3	-24.3	-17.7

I computed the change in average monthly surface solar

irradiance anomaly from one month to the next, δA. For example, for August to September for S3 - R2 path, δA = -17.7 - (-24.3)W/m^2 = 6.6 W/m^2 (Table 3.2). The values of δA are between 1.6 and 7.2 W/m^2. The standard deviation of δA is $\sqrt{2}$ * standard deviation of each monthly anomaly; namely $\sqrt{2} * 20\, W/m^2 \approx 29$. Thus values of the differences of the surface solar irradiance anomalies are not significantly different than zero. Based on this model, there is no significant change in the warming rate from the historical mean if surface solar irradiance anomalies is the only cause of changes in warming.

Spiesberger and Metzger (1991) used tomography to show that the warming between August 14 and September 14, 1987 was less than normal by 0.2°C±0.056°C in the upper 100 m along the path from S3 to R2 (Figure 2.1). If I assume that this change in warming was due only to changes in surface solar irradiance, I can compute the surface solar irradiance anomaly decrease over the month necessary to achieve this decrease in warming. Although not realistic, this assumption allows me to determine the magnitude of the surface solar irradiance anomalies necessary to change the warming by the above amount. Using the formula from Wyrtki and Uhrich (1982) to compute δT, the change in warming(°C) is:

$$\delta T = \frac{\delta H}{\rho C_p D} \qquad \textbf{(3.2)}$$

where ρ is the density of water (10^6 gm/m^3), C_p is the specific

heat capacity at constant pressure (4.2 J/gm °C), D is depth (100 m), and δH is the change in heating (J/m^2). For δT = -0.2°C ± 0.056°C this would result in $\delta H = -8.4 \times 10^7$ J/m^2 ± 2.35×10^7 W/m^2. To get this change in δH, I computed the necessary change in surface solar irradiance anomaly (δA) for 30 days with,

$$\delta A = \frac{\delta H(J/m^2)}{3600\,s/hour} \cdot \frac{1\,day}{24\,hour} \cdot \frac{1\,month}{30\,day} \quad . \qquad (3.3)$$

Equation 3.3 yields -32.4 W/m^2 ± 9.1 W/m^2 for a month. To get the results of Spiesberger and Metzger using only changes in the monthly surface solar irradiance would require a difference of -32.4 W/m^2 in the monthly anomalies from one month to the next.

For the above results I will consider two standard deviations away from each mean. This gives δA from tomography of -32.4 W/m^2 ± 18.2 W/m^2 and from the surface solar irradiance model δA is 6.6 W/m^2 ± 58 W/m^2. These values are less than two standard deviations apart.

I wish to restate that acoustic tomography measures a vertical slice of the ocean integrated along the acoustic path. Surface solar irradiance anomalies are a monthly average over a 9° grid of the ocean surface. The model considers only changes in surface solar irradiance and neglects changes in the advection and other heat budget terms. Changes in the neglected terms may dominate changes in warming.

Chapter IV

Discussion and conclusions

4.1 The Forward Model

We used the Levitus climatological data base with the Del Grosso sound speed algorithm to generate sound speed profiles as input to our forward model. The MPP ray trace program was used as the forward model. MPP produces both geometric and diffracted ray arrivals as output. We identified six eigen-rays for the spring, fall, and winter seasons and seven for the summer season.

We compared the MPP output for the spring and summer to the 1987 experiment data. The MPP forward model did a good job of predicting arrival times. The sound rays take about twenty minutes to travel between the source and receiver. MPP predicted their arrival time within 0.1 seconds(Table 2.2). Temperature fluctuations can account for a 0.1 s offset.

4.2 Variations in the Forward Model

The seasonal stability in the ray paths of the forward model was examined by computing the non-linearity in the travel time changes as a function of season. It was shown (Table 2.3) that there is a large percentage of non-linearity in the changes of travel time (>30%) between the seasons for most of the eigen-

rays using summer ray paths as the reference; the summer eigenray paths are not a good approximation for the other seasons for tomographic inversions.

4.3 The Observed Acoustic Data

The travel time decreases between year-day 140 and year-day 260. The change in travel time over the 120 day period is largest for the later arrivals(Figure 2.9). The later arrivals show decreases in total travel time which indicate faster sound speeds along the ray's trajectory. The later arrivals correspond to rays with smaller launch angles, that sample less of the near surface waters. Multipaths closest to the surface show much smaller changes in travel time. The earlier arrivals show an increase in travel time from year-day 140 to year-day 195 and then a decrease in travel time until the end of the experiment, year-day 260. An increase in travel time corresponds to slower sound speeds along the ray path, indicating cooler water.

4.4 Surface Solar Irradiance

The solar irradiance anomalies at the oceans surface, computed by Chertock, along the experiment's sound path range from -4 W/m^2 ± 20 W/m^2 to -35 W/m^2 ± 20 W/m^2. The magnitude of the surface solar irradiance anomalies shown in Figures 3.1 (a-f) are typically within the error limits of the surface solar irradiance data and so the changes in warming due to from them have no statistical significance.

I considered a simple model in which ocean temperature changes in the first 100 m of the water column are a function only of changes in the surface solar irradiance. The model does not consider changes in the other terms of the heat budget (section 1.3) nor does it consider advection. I computed the surface solar irradiance anomalies (using the model) necessary for the change in warming found by Spiesberger and Metzger. They derived the change in warming from tomographic inversions for the path they analyzed in the experiment area. They found below normal heating from August to September.

4.5 Conclusions

Surface solar irradiance is only one of four terms in the heat budget, the other three being long-wave radiation, sensible heat, and latent heat. We must also consider advection of heat when looking at the ocean's heat budget. No direct relationship between surface solar irradiance anomalies and travel time changes can be inferred without doing a complete heat budget including advection effects.

Acoustic tomography has been shown to be capable of measuring the thermal properties of the ocean on a basin scale, including inter-annual temperature variations (Spiesberger and Metzger, 1991; Spiesberger et al., 1992). A long term tomographic experiment covering the entire ocean, along with a heat budget computation including the terms discussed in section 1.3 and advection, would be important in measuring changes in warming of the ocean.

Ben-Menahem, A., and J.S. Sarva, Seismic Waves and Sources, Springer-Verlag, New York, 1108 pp, 1981

Brekhovskikh, L. and Y. Lysanov, Fundamentals of Ocean Acoustics. Springer Verlag, New York, 250 pp, 1982

Brown, M.G., Application of the WKBJ Green's function to acoustic propagation in horizontally stratified oceans, J. Acoust. Soc. Am., 71, 1427-1432, 1982

Chertock, B., Global monitoring of net solar irradiance at the ocean surface using Nimbus-7 satellite data. Doctoral Dissertation, Scripps Institution of Oceanography, University of California, San Diego, 118 pp, 1989

Chertock, B., R. Frouin, and C. Gautier, A technique for global monitoring of net solar irradiance at the ocean surface. Part II: Validation, J. Appl. Meteor., 31,1067-1083, 1992

Cornuelle, B, Inverse methods and results from the 1981 ocean acoustic tomography experiment. PH.D. Thesis, Massachusetts Institute of Technology/Woods Hole Oceanographic Institution, 359 pp, 1983

Cornuelle, B., C. Wunsch, D. Behringer, T. Birdsall, M. Brown, R. Heinmiller, R. Knox, K. Metzger, W. Munk, J. Spiesberger, R.

Spindel, D. Webb, and P. Worcester, Tomographic maps of the ocean mesoscale, Part 1: Pure acoustics, J. Phys. Oceanogr., 15, 133-152, 1985

Cornuelle, B., R. Heinmiller, R. Knox, K. Metzger, W. Munk, J. Spiesberger, R. Spindel, D. Webb, P. Worchester, and C. Wunsch, A Demonstration of Ocean Acoustic Tomography, Nature,299,121-125,1982

Defense Mapping Agency, Department of Defense World Geodetic System 1984: Its Definition and Relationships with local Geodetic Systems, 121 pp., Director of Defense Mapping Agency, U.S. Naval Observatory, Washington D.C., 1987

Del Grosso, V.A., New equation for the speed of sound in natural waters (with comparisons to other equations), J. Acoust. Soc. Am. 56, 1084-1091, 1974

Ewing, M., and J.L. Worzel, Propagation of sound in the ocean, III, Mem. Geol. Soc. Am., 27, 1-35, 1948

Frisk, G., Class notes, 13.861 Ocean and Seabed Acoustics I, 1991

Frouin, R. and B. Chertock, A technique for global monitoring of net solar irradiance at the ocean surface. Part I: Model, J. Appl. Meteor., 31, 1056-1066, 1992

Gill, A.E., Atmosphere-Ocean Dynamics,Academic Press. Inc., New York, 662 pp., 1982

Hamilton K.G., W.L. Siegmann and M.J. Jacobson, Simplified calculation of ray-phase perturbations to ocean-environmental variations, J. Acoust. Soc. Am., 67, 1193-1206, 1980

Hucek, R., H.L. Kyle, and P.E. Aradanuy, Nimbus 7 Earth Radiation Budget wide field of view climate data set improvement. 1. The earth albedo from deconvolution of shortwave measurements, J. Geophys. Res., 92, 4107-4123, 1987

Kyle, H.L., P.E. Ardanuy, and E.J. Hurley, The status of the Nimbus 7 earth-radiation-budget data set, Bull. Amer. Meteor. Soc., 66, 1378-1388, 1985

Kyle, H.L., K.L. Vasanth, and the Nimbus 7 ERB Experiment Team, Some characteristic differences in the earth's radiation budget over land and ocean derived from the Nimbus-7 ERB experiment. J. Climate Appl. Meteor., 25, 958-981, 1986

Levitus, S., Climatological Atlas of the World Ocean, NOAA Prof. Pap., 13, 173 pp., 1982

Liberatore, S.P., Modified Quad-M Interrogator, Internal report, Dep. of Appl. Ocean Phys. and Eng., Woods Hole Oceanogr. Inst., Woods Hole, Mass., 1985

Minnis, P., and E.F. Harrison, Diurnal variability of regional cloud and clear-sky radiative parameters derived from GOES data, Part III, November 1978 radiative parameters, J. Climate Appl. Meteor., 23, 1032-1051, 1984

Munk, W.H., and C. Wunsch, Ocean Acoustic Tomography: A Scheme for Large-Scale Monitoring, Deep Sea Res.,26,123-161,1979

NASA, Nimbus 7 Earth Radiation Budget (ERB) Matrix User's Guide, Volume I. Experiment Description and Quality Control Report for Year 1. NASA/Goddard Space Flight Center, Greenbelt, MD 20771, 121 pp, 1984a

NASA, Nimbus 7 Earth Radiation Budget (ERB) Matrix User's Guide, Volume II. Tape Specifications. NASA/Goddard Space Flight Center, Greenbelt, MD 20771, 40 pp, 1984b

National Geophysical Data Center, ETOPO5, 5 minute gridded world elevations and bathymetry - a digital data base, Boulder, Colo., 1987

Pierce, A.D., Acoustics: An introduction of its Physical Principles and Applications, McGraw-Hill, New York, 642 pp., 1981

Raschke, E., T.H. Vonder Haar, W.R. Bandeen, and M. Pasternak, The annual radiation balance of the earth-atmosphere system during 1969-70 from Nimbus 3 measurements, J. Atmos. Sci., 30, 341-364, 1973

Spiesberger, J., T. Birdsall, K. Metzger, R. Knox, C. Spofford, R. Spindel, Measurements of Gulf Stream Meandering and Evidence of Seasonal Thermocline Development using Long-Range Acoustic Transmissions, J. Physical Oceanography,13,1836-1846,1983

Spiesberger, J., P.J. Bushong, K. Metzger and T.G. Birdsall, Basin-Scale Tomography: Synoptic Measurements of a 4000 km Length Section in the Pacific. J. Phys. Ocean., 19, 1073-1090, 1989

Spiesberger, J., R.C. Spindel and K. Metzger, Stability and Identification of Ocean Acoustic Multipaths. J. Acoust. Soc. Am., 67, 2011-2017, 1980

Spiesberger, J., and K. Metzger, A New Algorithm for Sound Speed in Seawater, J. Acoust. Soc. Am., 89(6), 1991

Spiesberger, J., Ocean Acoustic Tomography: Travel Time Biases, J. Acoust. Soc. Am., 77, 83-100, 1985

Spiesberger, J., and P.F. Worcester, Perturbations in Travel Time and Ray Geometry due to Mesoscale Disturbances: A Comparison of Exact and Approximate Calculations, J. Acoust. Soc. Am., 74, 219-225, 1983

Spiesberger, J. and K. Metzger, Basin-scale tomography: A new tool for studying Weather and Climate, J. Geophysical Research,96,4869-4889, 1991

Spiesberger, J., K. Metzger, and J. Furgerson, Listening for climatic temperature change in the northeast Pacific: 1983-1989, JASA,92,384-396, 1992

Stewart, R. Methods of Satellite Oceanography, University of California Press, California, 360pp., 1985

Tanré, D., C. Deroo, P. Duhaut, M. Herman, J.J. Morcretee, J. Perbos, and P.Y. Deschamps, Simulation of the Satellite Signal in the Solar Spectrum (5S) Model User's Guide. Laboratoire d'Optique Atmosphérique, Université des Sciences et Techniques de Lille, 59655 Villeneuve d'Ascq Cedex, FRANCE, 259 pp, 1986

Tolstoy, I., and C.S. Clay, Ocean Acoustics, Theory and Experiment in Underwater Sound, McGraw-Hill, New York, 293 pp, 1966

Wallace, J., and P. Hobbs, Atmospheric Science, Academic Press, San Diego, 467 pp, 1977

Worcester, P.F., B. D. Dunshaw, and B.M. Howe, Proc. IEEE Fourth Working Conference on Current Measurement, Clinton, Maryland, 65-70, 1990

Wyrtki, K., and L. Uhrich, On the Accuracy of Heat Storage Computations, J. Phys. Oceanogr.,12,1411-1416, 1982